International Journal of Robotics and Control Systems
Vol. 5, No. 6, 2025, pp. 2669-2684
ISSN 2775-2658
http://pubs2.ascee.org/index.php/ijrcs

Raspberry Pi-Based Rapid Control Prototyping for PMSM Drive System Using RBFNN on OPAL-RT Platform

Quoc Vuong Pham [a,1], Trung Nhan Nguyen [a,2], Thanh Hai Tran [b,3], Bui Thi Cam Quynh [a,4], Thanh Quyen Ngo [a,5,*], Van Sy Nguyen [c,6], Tong Tan Hoa Le [a,7]

[a] Faculty of Electrical Engineering Technology, Industrial University of Ho Chi Minh City, Vietnam
[b] Office of Planning and Investment, Industrial University of Ho Chi Minh City, Vietnam
[c] Faculty of Automotive Engineering Technology, Industrial University of Ho Chi Minh City, Vietnam
[1] 23741191.vuong@student.iuh.edu.vn; [2] nguyentrungnhan@iuh.edu.vn; [3] tranthanhhai@iuh.edu.vn; [4] buithicamquynh@iuh.edu.vn; [5] ngothanhquyen@iuh.edu.vn; [6] nguyenvansy@iuh.edu.vn; [7] letongtanhoa@iuh.edu.vn
* Corresponding Author

ARTICLE INFO

Article history
Received September 25, 2025
Revised October 29, 2025
Accepted November 24, 2025

Keywords
PMSM;
Raspberry Pi;
Adaptive Control;
RBFNN;
OPAL-RT

ABSTRACT

This study addresses the challenge of improving speed control accuracy and noise immunity in permanent magnet synchronous motor (PMSM) drive systems, which are widely used in industrial applications requiring high drive efficiency. Conventional controllers such as PIDs exhibit limitations in handling nonlinear components, parameter uncertainties, and time-varying dynamics. To overcome these issues, a sliding mode control (SMC) strategy integrated with a radial basis function neural network (RBFNN) is proposed. The RBFNN adaptively estimates and compensates for unknown components in real time, while the overall stability of the system is rigorously proven using Lyapunov theory. The proposed control algorithm is developed in MATLAB/Simulink, validated through real-time simulation using OPAL-RT OP5707XG platform and implemented on Raspberry Pi hardware under the Rapid Control Prototype (RCP) framework. The control structure consists of a speed control loop enhanced by adaptive RBFNN and a flux-driven current control loop. Experimental results under multi-stage variable speed conditions demonstrate that the proposed controller achieves fast dynamic response, minimal steady-state error, reduced overshoot and high robustness to load variations and disturbances.

© 2025 The Authors.
Published by Association for Scientific Computing Electrical and Engineering.
This is an open-access article under the CC-BY-NC license.

1. Introduction

The electric propulsion system is one of the most critical components of an electric vehicle (EV), consisting of an electric drive, an energy storage system, and a transmission unit. A typical propulsion drive is expected to deliver high energy density along with fast dynamic response, while ensuring compatibility with vehicle requirements such as optimum acceleration, high torque, efficient speed control, and reliable gradability [1]. The overall energy conversion efficiency of an electric propulsion system depends on several factors, including machine losses, harmonic distortion, torque pulsations, and cogging torque. Therefore, recent research has increasingly focused on improving the energy efficiency of EVs, drawing on energy-saving strategies traditionally applied in industrial motor applications [2]. Although direct current (DC) motors are structurally simple and suitable for low-speed applications, their drawbacks—including low efficiency, bulky construction, and reduced

reliability due to brushes and commutators—result in high maintenance requirements and challenges in achieving accurate low-speed control [3]. Switched reluctance motors (SRMs) offer advantages such as robustness, high starting torque, and simple construction but are hindered by considerable torque ripple and acoustic noise [4]. Induction motors (IMs), conversely, are well-known for their durability, quiet operation, ease of maintenance, and reliable high-speed performance, though their control systems are comparatively complex. Brushless DC motors (BLDCs) are structurally similar to PMSMs, differing mainly in excitation: BLDCs use trapezoidal waveforms, whereas PMSMs use sinusoidal waveforms. This distinction grants PMSMs higher efficiency, better power density, and lower torque ripple, making them the leading choice for high-performance EV applications [5]–[7].

PMSMs have attracted significant attention in modern motor control research owing to their inherent merits, including compact design, high power density, elevated efficiency, and excellent controllability [8]–[10]. Among the various control strategies, Field-Oriented Control (FOC) has emerged as the most widely adopted approach in industrial drives and automation applications, primarily due to its advantages of reduced torque ripple, fast transient response, and high control precision. The FOC framework is typically realized through a dual closed-loop architecture, comprising an outer speed loop—responsible for shaping the system's dynamic behavior—and an inner current loop—ensuring both transient performance and steady-state accuracy. In this structure, the speed loop design must simultaneously consider tracking accuracy and robustness against disturbances. Conventional implementations generally rely on proportional–integral (PI) control; nevertheless, the linear characteristics of PI inherently conflict with the nonlinear dynamics of PMSMs, thereby limiting its ability to achieve the stringent requirements of high-performance applications [11]. Addressing these disturbances remains a critical issue for ensuring accurate and stable PMSM operation in EV systems.

PMSMs exhibit nonlinear and strongly coupled electromechanical dynamics, which make their control inherently challenging. Conventional linear control techniques often fail to ensure satisfactory performance because of intrinsic nonlinearities, parameter uncertainties, torque ripple, and high sensitivity to external disturbances. These characteristics limit both the precision and efficiency of PMSM drives under real operating conditions. A variety of nonlinear control strategies have been proposed to improve system controllability, including Model Predictive Control (MPC) [12], Fuzzy Logic Control [13], Active Disturbance Rejection Control (ADRC) [14], [15], and Data-Driven Event-Triggered Adaptive Dynamic Programming Control [16], [17]. These approaches show good potential, particularly when the mathematical model of the motor is incomplete or imprecise. However, their success strongly depends on accurate modeling and parameter tuning, which often complicates practical implementation.

Advanced control frameworks such as adaptive control [18], [19], robust control [20], sliding mode control (SMC) [21], [22], disturbance rejection control [23], and estimation-based disturbance observers [24], [25] have also been extensively investigated. Among them, SMC has gained significant attention for its robustness against parameter variations, strong disturbance rejection, and fast transient response [26]–[32]. Nevertheless, its practical use is hindered by the inherent chattering phenomenon, which can cause high-frequency oscillations, mechanical wear, and even instability. In addition, the requirement for accurate mathematical modeling and parameter identification makes implementation on embedded hardware platforms more complex [33], [34]. Several techniques have been developed to mitigate these limitations, such as redesigning the sliding surface, employing smooth approximation functions (e.g., replacing the signum function with a saturation function), or integrating SMC with intelligent and soft computing methods [35]–[38]. Recent studies on fractional-order SMC introduce additional degrees of freedom in controller design, allowing better trade-offs between robustness and performance [39]–[41]. Thanks to its simple structure, strong disturbance rejection, and adaptability to nonlinear dynamics, SMC remains one of the most reliable control techniques for PMSM drive systems requiring high precision and robustness [42]–[48].

The development of compact computers such as Raspberry Pi has facilitated flexible and low-cost solutions for applications. Due to its support for multiple programming languages, ease of

integration, and small size, Raspberry Pi has been widely used in projects related to robot control, cloud-based communication, and surveillance systems. Several studies highlight its utility in intelligent robotics: human tracking through computer vision [49], sensor data collection in mobile robots [50], visual servoing using video cameras [51], [52], and cloud-enabled robotics [53]. Raspberry Pi has also been applied in wireless robot control [54], [55], low-cost mobile and educational robots integrating Arduino [56], [57], autonomous vehicles with vision-based tracking capabilities [58], and remote operation of robotic arms via a web interface [59]. These works confirm that Raspberry Pi is a reliable platform for the authors to decide to use in this research.

In this study, the authors deploy Raspberry Pi to handle uncertain components through radial basis function neural networks (RBFNN) [60]. Thanks to its global learning properties and strong adaptability, RBFNN proves to be particularly effective in dealing with nonlinear, unmodeled factors as well as external disturbances in control systems such as electric drives or robot control. In addition, integrating RBFNN with online learning algorithms also opens up the prospect of significantly improving control performance, thanks to the ability to update parameters in real time, ensuring convergence and fast response under changing operating conditions [61]. The main research contributions of this paper are:

1. RBFNN is built to approximate a part of the mathematical model of the system that is not known in advance.
2. Experiments were conducted on the OPAL-RT platform with two different speed change scenarios to demonstrate the feasibility of the proposed method.
3. The proposed method is implemented on Raspberry Pi 4B and verified in real time on OPAL-RT simulation platform. The data exchange between the controller and the simulator is performed using Modbus protocol, thereby demonstrating the feasibility of the rapid control prototyping solution for PMSM drive system using the proposed method.

The structure of the paper is as follows. Section 2 presents the mathematical model of the PMSM. The proposed controller is described in detail in Section 3. Section 4 reports the experimental results used to validate the effectiveness of the control scheme. Conclusions are summarized in Section 5.

2. System description

2.1. First-Order Mathematical Model of the PMSM Drive System

The mathematical model of the object is defined as follows [62]–[64]:

$$\begin{cases} i_d = -\dfrac{R_s}{L} + n_p \omega i_q + \dfrac{u_d}{L} \\ i_q = -n_p \omega i_d - \dfrac{R_s}{L} i_q - \dfrac{n_p \varphi_f}{L} \omega + \dfrac{u_q}{L} \\ \dot{\omega} = \dfrac{K_t}{J} i_q - \dfrac{B}{J} \omega - \dfrac{T_L}{J} \end{cases} \tag{1}$$

where i_d and i_q are the $d-q$ axis currents, u_d and u_q are the $d-q$ axis voltages, R_s is the stator resistance, J is the rotor moment of inertia, ω is the rotor angular speed, T_L is the load torque, B is the viscousfriction coefficient, L is the stator inductor, φ_f is the rotor flux linkage, n_p is the pole pairs, $K_t = 1.5 n_p \varphi_f$ is the torque constant. Simplifying the third equation in (1) gives:

$$\dot{\omega} = b i_q + a(t) \tag{2}$$

where $b = \frac{1.5 n_p \varphi_f}{J}$, $a(t) = -\frac{B}{J}\omega - \frac{T_L}{J}$. By applying Laplace transform to (2) it should be rewritten:

$$s\Omega(s) = bI_q(s) + A(s) \tag{3}$$

where s is a complex variable in the frequency domain. The parameters $\Omega(s)$, $I_q(s)$ and $A(s)$ are determined through the Laplace transform of the quantities ω, i_q and $a(t)$ respectively. When designing the controller for the speed loop, the actual q–axis current is replaced by the q–axis reference current. Therefore:

$$\dot{\omega} = bi_q^* + a(t) \tag{4}$$

The PMSM drive system based on the FOC of the rotor as shown in Fig. 1, consists of one speed control loop and two current control loops. In order to achieve the separation between speed and current and maximize the ratio between them, the shaft reference current i_d^* is set to 0. In this structure, the two current control loops of the PMSM speed regulation system are realized by two PI controllers. The relationship between the speed of the PMSM and the reference q–axis current i_q^* can be approximately described through the PMSM model presented above.

2.2. Second-Order Mathematical Model of the PMSM Drive System

A second-order mathematical model of i_q^* and PMSM speed is constructed to optimize the closed-loop performance of the drive system, especially in cases requiring high precision. The transfer function of the PI controller in the q–axis current loop can be determined as follows by observing the signal propagation direction of the d–axis current loop in Fig. 1.

$$\frac{U_q(s)}{I_q^*(s) - I_q(s)} = k_p + \frac{k_i}{s} \tag{5}$$

where k_p and k_i are the proportional and integral gains of the PI controller in the q–axis current control loop, respectively. $I_q(s)$, $I_q^*(s)$ and $U_q(s)$ are the Laplace transforms of i_q, i_q^* and u_q respectively. Equation (5) can be rewritten as follows:

$$I_q(s) = I_q^*(s) - \frac{U_q(s)}{k_p + \frac{k_i}{s}} \tag{6}$$

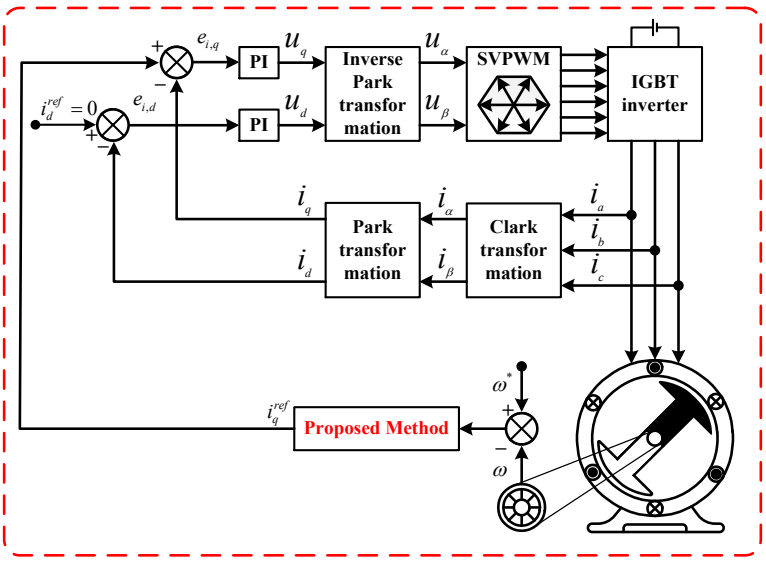

Fig. 1. An illustration of the control block diagram corresponding to the proposed method for PMSM

Equation (3) is rewritten as follows:

$$\left(s^2+\frac{k_i}{k_p}s\right)\Omega(s)=\left(s+\frac{k_i}{k_p}\right)\left(bI_q(s)+A(s)\right) \tag{7}$$

Substituting (6) into (7) can be obtained as follows:

$$\left(s^2+\frac{k_i}{k_p}s\right)\Omega(s)=\left(bs+\frac{bk_i}{k_p}\right)I_q^*(s)-\frac{bs}{k_p}U_q(s)+\left(s+\frac{k_i}{k_p}\right)A(s) \tag{8}$$

$U(s)$ is defined as follows to simplify the equation:

$$U(s)=b\left(s+\frac{k_i}{k_p}\right)I_q^*(s) \tag{9}$$

Therefore (8) is simplified as follows:

$$\left(s^2+\frac{k_i}{k_p}s\right)\Omega(s)=U(s)-\frac{bs}{k_p}U_q(s)+\left(s+\frac{k_i}{k_p}\right)A(s) \tag{10}$$

The transfer function from (9) can be rewritten as:

$$I_q^*(s)=\frac{k_p}{b(k_ps+k_i)}U(s) \tag{11}$$

Applying the inverse Laplace transform to (10), the equation is rewritten as follows:

$$\ddot{\omega}=u-\frac{k_i}{k_p}\dot{\omega}-\frac{b}{k_p}\dot{u}_q+\dot{a}(t)+\frac{k_i}{k_p}a(t) \tag{12}$$

From the above equation, the second-order model of PMSM has been successfully constructed, in which u is the inverse Laplace transform of $U(s)$.

The error between the reference speed ω^* and the actual speed ω of the PMSM is used to define the system state variable as follows:

$$x_1=\omega-\omega^* \tag{13}$$

Let $x_2=\dot{\omega}-\dot{\omega}^*$ and substitute (12) into the second derivative of (13) to get:

$$\begin{cases}\dot{x}_2=u-\ddot{\omega}^*-\left(\frac{k_i}{k_p}+\frac{B}{J}\right)\dot{\omega}-\frac{k_iB}{k_pJ}\omega+d\\ d=-\frac{b}{k_p}\dot{u}_q-\frac{\dot{T}_L}{J}-\frac{k_i}{Jk_p}T_L\end{cases} \tag{14}$$

The PMSM drive system can be simplified based on (13) and (14) as follows:

$$\begin{cases}\dot{x}_1=x_2\\ \dot{x}_2=f+gu+d=-\ddot{\omega}^*-\frac{k_iB}{k_pJ}\omega-\left(\frac{k_i}{k_p}+\frac{B}{J}\right)\dot{\omega}+u+d\end{cases} \tag{15}$$

where the disturbance of the PMSM drive system is represented by d. Besides, the variable u defined in (9) and (11), acts as the intermediate variable of the controller in the speed loop of the PMSM drive system.

3. Controllers Design

The sliding surface of the system is defined as follows:

$$s = \dot{e} + ce \tag{16}$$

with $c \geq 1$. Then:

$$\dot{s} = \ddot{e} + c\dot{e} = \ddot{\omega}^* - \ddot{\omega} + c\dot{e} = \ddot{\omega}^* - f - u - d + c\dot{e} \tag{17}$$

The control law can be designed as follows if f is known exactly:

$$u = \frac{1}{g}[-f + \ddot{\omega}^* + c\dot{e} + \eta sgn(s)] \tag{18}$$

By substituting (18) into (17), (17) can be rewritten as follows:

$$\dot{s} = \ddot{e} + c\dot{e}$$

$$\dot{s} = \ddot{\omega}^* - \ddot{\omega} + c\dot{e}$$

$$\dot{s} = \ddot{\omega}^* - f - u - d + c\dot{e}$$

$$\dot{s} = -\eta sgn(s) - d \tag{19}$$

If $\eta \geq d$ is chosen then:

$$s\dot{s} = -\eta \mid s \mid -sd \leq 0 \tag{20}$$

In case f is not known exactly, estimation needs to be carried out through different methods. In this study, RBF neural network is used to approximate the uncertain component f. The RBF neural network consists of an input layer $\underline{\boldsymbol{x}} = [x_1, x_2, \ldots, x_n]^T$, a hidden layer $\boldsymbol{H}(\underline{\boldsymbol{x}}) = [h_1, h_2, \ldots, h_m]^T$, a weight vector $\boldsymbol{W} = [w_1, w_2, \ldots, w_m]^T$, and an output layer y.

$$h_j = exp\left(-\frac{\|\underline{\boldsymbol{x}} - \boldsymbol{c}_j\|^2}{2b_j^2}\right), j = 1,2, \ldots,5 \tag{21}$$

The RBF neural network is used to estimate the f component:

$$f = \boldsymbol{W}^{*T}\boldsymbol{H}(\underline{\boldsymbol{x}}) + \varepsilon \tag{22}$$

where $\boldsymbol{x} = [e, e_{i,q}]^T$ is the input, i is the input number, j is the number of hidden layer, $h = [h_j]^T$ is the output of the Gaussian function, $\boldsymbol{W}^*$ is the ideal weight of the neural network, ε is the approximate error of the RBFNN and $\varepsilon \leq \varepsilon_N$. Each neuron applies a Gaussian activation function, whose center vector is $\boldsymbol{c}_j = \left[c_{1j}, c_{2j}\right]^T$ and width is b_j. With these parameters of the Gaussian function, the real-time neural network output can then be expressed as follows:

$$\hat{f} = \widehat{\boldsymbol{W}}^T\boldsymbol{H}(\underline{\boldsymbol{x}}) \tag{23}$$

where $\hat{f}$ is an approximation of the f component, and $\widehat{\boldsymbol{W}}^T = [\widehat{w}_1, \widehat{w}_2, \ldots, \widehat{w}_5]^T$ is the adaptive weight matrix. Then (18) is rewritten as follows:

$$u = \frac{1}{g}\left[-\hat{f} + \ddot{\omega}^* + c\dot{e} + \eta sgn(s)\right] \tag{24}$$

Proof. The Lyapunov function is defined as follows:

$$L = \frac{1}{2}s^2 + \frac{1}{2\gamma}\widetilde{\boldsymbol{W}}^T\widetilde{\boldsymbol{W}} \tag{25}$$

where $\widetilde{\boldsymbol{W}} = \boldsymbol{W}^* - \widehat{\boldsymbol{W}}$. Using (17) and (24) substitute into the derivative of (25):

$$\dot{L} = s\dot{s} + \frac{1}{\gamma}\widetilde{\boldsymbol{W}}^T\dot{\widetilde{\boldsymbol{W}}} = s(\ddot{\omega}^* - \ddot{\omega} + c\dot{e}) - \frac{1}{\gamma}\widetilde{\boldsymbol{W}}^T\dot{\widehat{\boldsymbol{W}}}$$

$$\dot{L} = s(\ddot{\omega}^* - f - u - d + c\dot{e}) - \frac{1}{\gamma}\widetilde{\boldsymbol{W}}^T\dot{\widehat{\boldsymbol{W}}}$$

$$\dot{L} = s\left\{\ddot{\omega}^* - f - \frac{1}{g}\left[-\hat{f} + \ddot{\omega}^* + c\dot{e} + \eta sgn(s)\right] - d + c\dot{e}\right\} - \frac{1}{\gamma}\widetilde{\boldsymbol{W}}^T\dot{\widehat{\boldsymbol{W}}}$$

$$\dot{L} = s\left[\ddot{\omega}^* - f + \hat{f} - \ddot{\omega}^* - c\dot{e} - \eta sgn(s) - d + c\dot{e}\right] - \frac{1}{\gamma}\widetilde{\boldsymbol{W}}^T\dot{\widehat{\boldsymbol{W}}}$$

$$\dot{L} = s\left[-\tilde{f} - \eta sgn(s) - d\right] - \frac{1}{\gamma}\widetilde{\boldsymbol{W}}^T\dot{\widehat{\boldsymbol{W}}}$$

$$\dot{L} = s\left[-\widetilde{\boldsymbol{W}}^T\boldsymbol{H}(\underline{\boldsymbol{x}}) - \varepsilon - \eta sgn(s) - d\right] - \frac{1}{\gamma}\widetilde{\boldsymbol{W}}^T\dot{\widehat{\boldsymbol{W}}}$$

$$\dot{L} = -s\widetilde{\boldsymbol{W}}^T\boldsymbol{H}(\underline{\boldsymbol{x}}) - s\varepsilon - s\eta sgn(s) - sd - \frac{1}{\gamma}\widetilde{\boldsymbol{W}}^T\dot{\widehat{\boldsymbol{W}}}$$

$$\dot{L} = -\widetilde{\boldsymbol{W}}^T\left[s\boldsymbol{H}(\underline{\boldsymbol{x}}) + \frac{1}{\gamma}\dot{\widehat{\boldsymbol{W}}}\right] - s[\varepsilon + d + \eta sgn(s)] \tag{26}$$

where $\tilde{f} = \hat{f} - f = \boldsymbol{W}^{*T}\boldsymbol{H}(\underline{\boldsymbol{x}}) + \varepsilon - \widehat{\boldsymbol{W}}^T\boldsymbol{H}(\underline{\boldsymbol{x}}) = \widetilde{\boldsymbol{W}}^T\boldsymbol{H}(\underline{\boldsymbol{x}}) + \varepsilon$. The adaptive law is defined as follows:

$$\dot{\widehat{\boldsymbol{W}}} = -\frac{1}{\gamma}s\boldsymbol{H}(\underline{\boldsymbol{x}}) \tag{27}$$

The result obtained after substituting (27) into (26):

$$\dot{L} = -s[\varepsilon + d + \eta sgn(s)]$$

$$\dot{L} = -s(\varepsilon + d) - \eta|s| \tag{28}$$

Based on (27), if ε is limited and $\eta \geq \varepsilon_N + d$ then $\dot{L} \leq 0$. Consequently, as time approaches infinity, the system parameters asymptotically converge to zero, ensuring complete stability of the overall system.

Fig. 2 depicts the overall structure of the experimental system based on Real-Time Digital Simulator using OP5707XG device. This model connects and synchronizes data through TP-Link TL-SF1005D network switch as the communication center between the components. At the signal processing and monitoring side, the computer performs the functions of observing, analyzing waveforms and simulation results. Besides, a Raspberry Pi 4 Model B (8 GB RAM) is connected to implement RBFNN algorithms to approximate the f component in this study.

4. Experimental results

In this section, two experimental scenarios are designed to validate the performance of the RBFNN-based controller for the PMSM drive system. In the first scenario, the controller is implemented on the Raspberry Pi platform, while the PMSM model is implemented on the OPAL-RT 5707 real-time simulation system, thereby evaluating the feasibility and stability of the control method. The next scenario focuses on speed variation experiments with different changing conditions and compares them with other controllers. All experiments aim to demonstrate the speed tracking ability and reliability of the proposed controller under different operating situations. The parameters of the PMSM used in all the scenarios are presented in Table 1, which are consistent with the values described in Section 2.

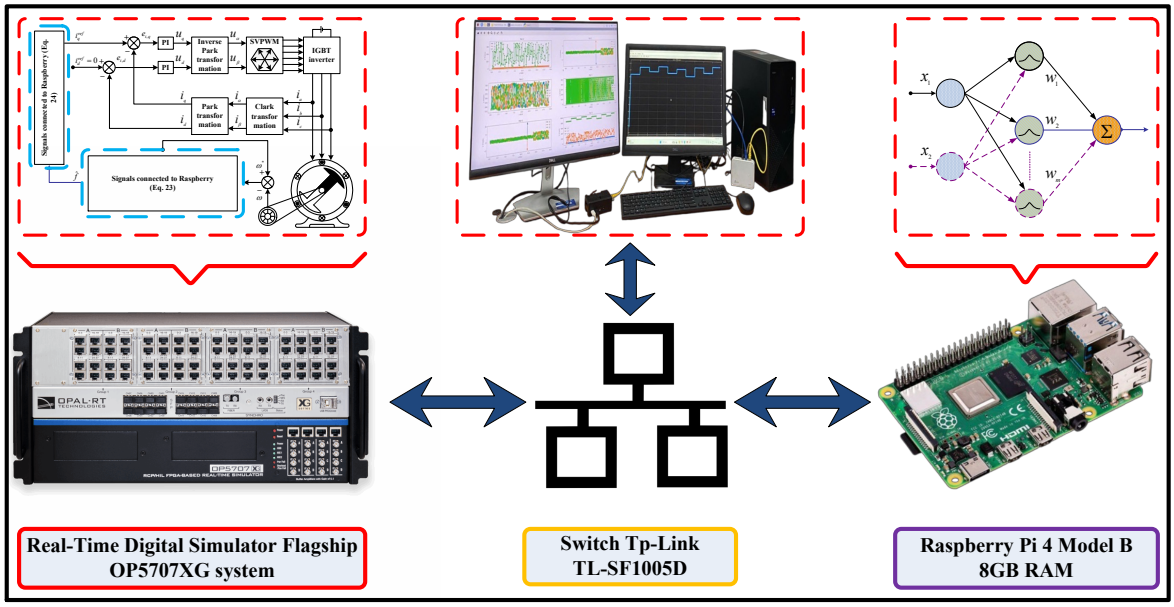

Fig. 2. Experimental systems in researches

Table 1. PMSM parameters used in the experiment

Parameter	Value
Moment of inertia (B)	$3.5 \times 10^{-4} kg \cdot m^2$
Viscous damping coefficient (B)	$7.21 \times 10^{-5} N \cdot m \cdot s/rad$
Stator resistance (R)	1Ω
Stator inductor (L)	$6.25 \times 10^{-3} H$
Permanent magnet flux (φ_f)	$0.32 Wb$
Number of pole-pairs (n_p)	4

The RBFNN parameters were configured to match the nonlinear dynamics and control bandwidth of the PMSM system. Their values, shown in Table 2, were derived from the authors' prior experimental investigations and fine-tuned to achieve stable convergence and robust performance in real-time implementation.

The real-time digital simulator flagship OP5707XG (Fig. 3) is employed to emulate the PMSM drive system with high fidelity and real-time performance. The OP5707XG, developed by OPAL-RT, integrates an 8-core Intel Xeon processor and a Xilinx Kintex-7 FPGA, offering superior computing power, low latency, and flexible I/O interfaces suitable for industrial control research. Leveraging these capabilities, the PMSM drive system and inverter are implemented on OP5707XG, while the proposed RBFNN-based controller is deployed on a Raspberry Pi platform for rapid control prototyping. The combination enables hardware-in-the-loop validation of the control strategy,

ensuring real-time stability and robustness, and providing a solid foundation for future practical applications.

Table 2. RBFNN parameters used in the experiment

Parameter	Value
n_j	5
η	0.5
γ	0.5
c	[-1 1]
b	1

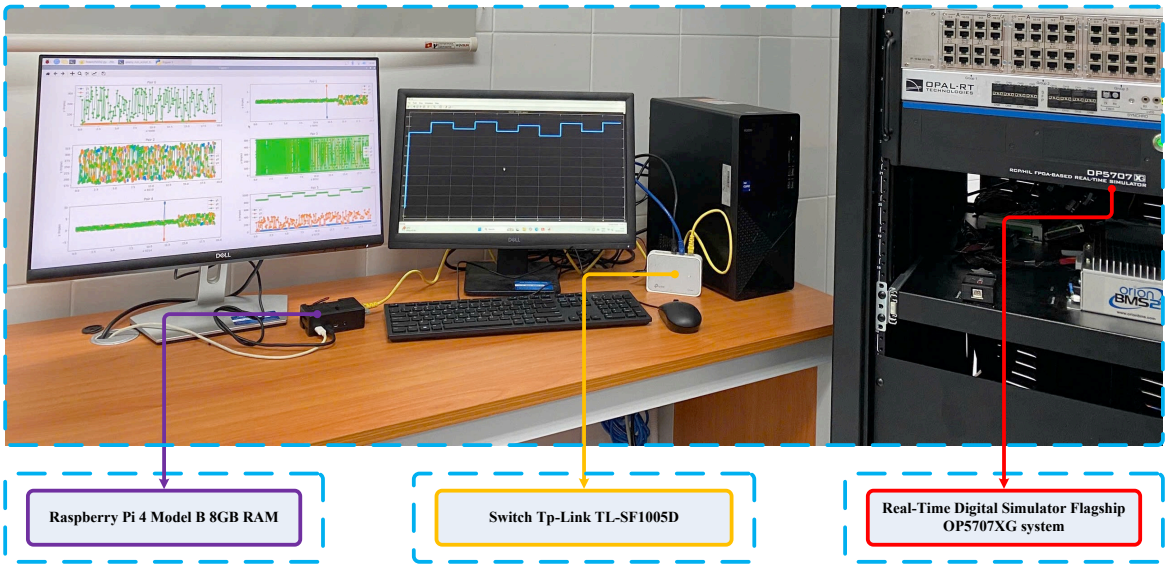

Fig. 3. Real-time digital simulator flagship OP5707XG system

4.1. Scenario 1

The experimental validation was carried out using PMSM to evaluate the speed tracking performance and robustness of the proposed control strategy. The PMSM model was implemented in MATLAB/Simulink, while the designed controller was deployed in real time on a Raspberry Pi platform to perform hardware-in-the-loop (HIL) testing. During a 20-second test, the reference speed was varied every 2 seconds to examine the dynamic response and adaptability of the system under different operating conditions. The actual rotor speed was continuously measured and compared with the reference trajectory to assess the tracking accuracy, rise time, and steady-state stability. Additionally, motor phase current, control voltage, and electromagnetic torque signals were recorded for further analysis of the transient and steady-state behaviors. To evaluate the disturbance rejection capability, a sudden external load torque was applied at the 14th second of the experiment. The system's ability to maintain stable operation and recover quickly from the disturbance demonstrates the robustness and effectiveness of the proposed RBFNN–SMC control scheme.

Fig. 4 shows the speed response of the PMSM motor controlled by the RBFNN controller. In Fig. 4-(a), the black line denotes the reference speed signal, while the red line represents the actual speed signal. The enlarged view highlights the fast and stable response of the controller whenever the reference speed changes. Fig. 4-(b) illustrates the time-domain variation of the speed error during the reference speed switching, which occurs every 2 seconds and rapidly converges to near zero afterward.

Fig. 5 shows the current response of the PMSM motor during the 20-second experiment, with the reference speed changed every 2 seconds and a sudden load applied at the 14th second. In Fig. 5-(a), the d–axis current (i_d) remains close to zero throughout the process. The q–axis current (i_q) changes

significantly at the times of changing the reference speed, playing the role of generating electromagnetic torque for the motor. In particular, when the sudden load is applied at the 14th second, i_q appears to fluctuate momentarily but quickly stabilizes again, demonstrating the robustness of the RBFNN controller. In Fig. 5-(b), the three stator currents i_{abc} have sinusoidal waveforms, 120° out of phase with each other, which correctly represents the balance characteristic of a three-phase system. During the 20-second experiment, the amplitude of the three-phase currents changes correspondingly to the change of the reference speed (every 2 seconds). In particular, at the 14th second when the load is suddenly applied, the three-phase waveform shows an instantaneous sharp amplitude, demonstrating the system's quick response to compensate for the load. However, the phase balance is still maintained, and the current waves quickly return to a steady state.

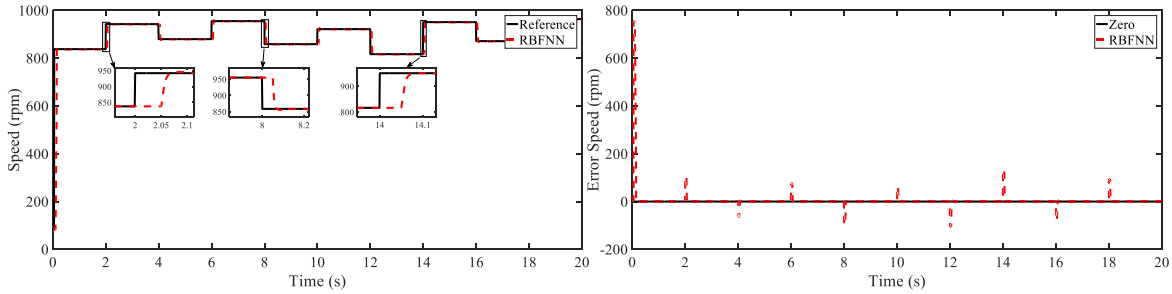

Fig. 4. Speed response (a) and speed error (b) of PMSM control system

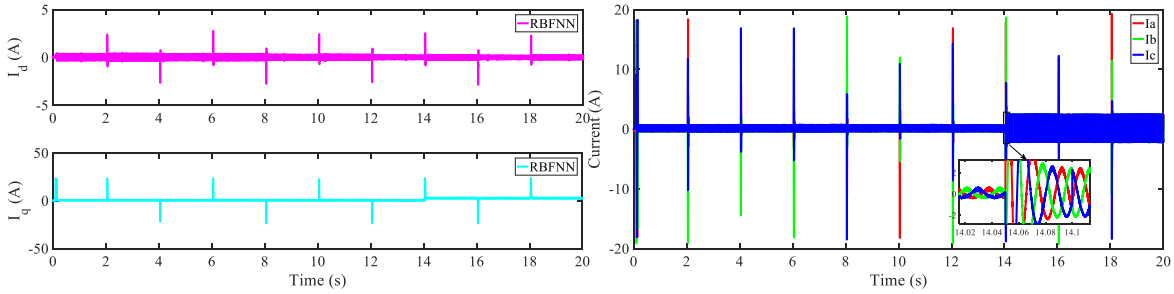

Fig. 5. Current control performance using the RBFNN controller

4.2. Scenario 2

In this scenario, the hardware setup and control implementation remain identical to those described in the previous experiment. The total duration of the experiment is 20 seconds, during which the reference speed profile is adjusted every 4 seconds to evaluate the controller's ability to handle slower dynamic transitions. At 14 seconds, an external load disturbance is intentionally applied to the motor shaft, similar to the previous scenario, to further evaluate the system's adaptability and disturbance rejection performance. The resulting responses in terms of motor speed, current, and electromagnetic torque are recorded to analyze the accuracy of the proposed controller.

Fig. 6 shows the simulation results of the speed response of PMSM with three different controllers. In the Fig. 6-(a), the black line is the reference signal, while the green (PID), blue (FOPID) and red (RBFNN) lines show the actual speed response, respectively. It can be seen that all three controllers follow the reference signal, but with different accuracy and transition times. The PID controller has larger oscillation and stall error; the FOPID controller improves the oscillation but still has deviation; meanwhile, the RBFNN controller gives fast, stable response and almost exactly matches the reference speed. In the Fig. 6-(b), the speed error of the controllers is shown more clearly. The results show that the error of PID fluctuates greatly and takes a long time to disappear. The FOPID has smaller error but still has a certain oscillation amplitude. In contrast, the error of RBFNN remains

very small and quickly returns to near zero after speed changes or when subjected to load at 14 seconds.

The 3D graph in Fig. 7 compares the RMS, Mean Error and MAE indices of the three controllers PID, FOPID and RBFNN, it can be seen that the RBFNN controller gives lower indices than the other controllers. The RMS and MAE values of RBFNN are the lowest among the three controllers, indicating that the proposed method operates more stably, with less oscillation and smaller error in the whole control process. The Mean Error value of RBFNN is also at the lowest level, demonstrating that the ability to track the set signal is high and the static error is almost eliminated. Compared with other controllers, PID gives a stable response but is still slow and the accuracy is not high, while FOPID improves significantly over PID thanks to its more flexible tuning characteristics. However, both of them do not achieve the same adaptability and efficiency as RBFNN.

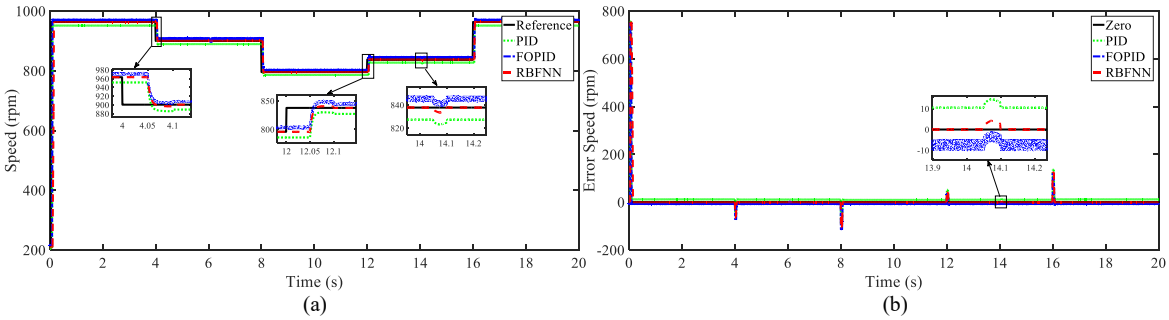

Fig. 6. Comparison of speed response (a) and speed error (b) between controllers

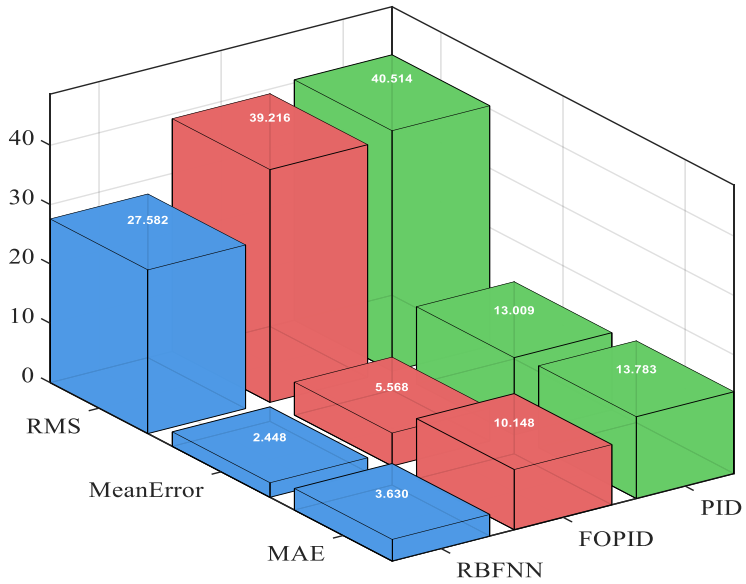

Fig. 7. Comparison index between controllers

5. Conclusion

This study proposes an SMC strategy combined with an RBFNN to improve the speed control accuracy of PMSM. RBFNN is used to estimate and compensate for unknown components of the motor model, while the SMC structure ensures robustness against parameter variations and external disturbances. The global stability of the system is proven through Lyapunov theory. The controller is validated through MATLAB/Simulink simulation and experimentally implemented on the OPAL-RT OP5707XG loop hardware platform combined with a Raspberry Pi-based rapid control prototyping system. Experimental results show that the proposed controller achieves fast dynamic response and

noise cancellation, improving accuracy compared to PID and FOPID controllers. However, the method still has some limitations, including the computational burden during online adaptation of the RBFNN network and sensitivity to parameter initialization. In addition, the choice of parameters should be appropriate to the processing capabilities of the Raspberry Pi, because if the value is too significant, it may lead to losing feedback data due to processing overload. In the future, the research will focus on optimizing the adaptive law to improve the convergence speed, extending the control structure to current control and multi-motor systems, and experimental verification in electric vehicle drive systems under various operating conditions.

Author Contribution: All authors contributed equally to the main contributor to this paper. All authors read and approved the final paper.

Acknowledgment: The author would like to sincerely thank the Faculty of Automotive Engineering Technology, Ho Chi Minh City University of Industry, for investing and supporting the Real-Time Digital Simulator Flagship OP5707XG equipment and the facilities that helped the author carry out this research.

Conflicts of Interest: The authors declare no conflict of interest.

References

[1] X. Han, D. Jiang, T. Zou, R. Qu, and K. Yang, "Two-segment three-phase PMSM drive with carrier phase-shift PWM for torque ripple and vibration reduction," *IEEE Transactions on Power Electronics*, vol. 34, no. 1, pp. 588–599, 2019, https://doi.org/10.1109/TPEL.2018.2824808.

[2] R. Yan, D. Wang, C. Wang, W. Miao, and X. Wang, "Analytical approach and experimental validation of sideband electromagnetic vibration and noise in PMSM drive with voltage-source inverter by SVPWM technique," *IEEE Transactions on Magnetics*, vol. 61, no. 1, pp. 1–6, 2024, https://doi.org/10.1109/TMAG.2024.3498051.

[3] H. Cao, Y. Deng, J. Liu, Y. Zuo, X. Liu, H. Wang, and C. H. T. Lee, "Improved deadbeat predictive current control of PMSM drives with repetitive control-based disturbance correction observer," *IEEE Transactions on Power Electronics*, vol. 40, no. 1, pp. 801–812, 2025, https://doi.org/10.1109/TPEL.2024.3482315.

[4] T. Yazdan, M. Humza, and H.-W. Cho, "Three-phase dual-winding multitasked PMSM machine using double layer concentrated winding for HEV application," *IEEE Access*, vol. 11, pp. 36682–36691, 2023, https://doi.org/10.1109/ACCESS.2023.3264568.

[5] S. Thangavel, D. Mohanraj, T. Girijaprasanna, S. Raju, C. Dhanamjayulu, and S. M. Muyeen, "A comprehensive review on electric vehicle: battery management system, charging station, traction motors," *IEEE Access*, vol. 11, pp. 20994–21019, 2023, https://doi.org/10.1109/ACCESS.2023.3250221.

[6] M. R. Khowja, K. Singh, A. la Rocca, G. Vakil, R. Ramnathan, and C. Gerada, "Fault-tolerant dual channels three-phase PMSM for aerospace applications," *IEEE Access*, vol. 12, pp. 126845–126857, 2024, https://doi.org/10.1109/ACCESS.2024.3451705.

[7] W. Deng, X. Zhang, and B. Yan, "An enhanced discrete virtual vector-based direct torque control of PMSM drives," *IEEE Transactions on Energy Conversion*, vol. 39, no. 1, pp. 277–286, 2024, https://doi.org/10.1109/TEC.2023.3314521.

[8] Z. Shi, X. Sun, Y. Cai, and Z. Yang, "Robust design optimization of a five-phase PM hub motor for fault-tolerant operation based on taguchi method," *IEEE Transactions on Energy Conversion*, vol. 35, no. 4, pp. 2036–2044, 2020, https://doi.org/10.1109/TEC.2020.2989438.

[9] X. Sun, C. Hu, G. Lei, Y. Guo, and J. Zhu, "State feedback control for a PM hub motor based on grey wolf optimization algorithm," *IEEE Transactions on Power Electronics*, vol. 35, no. 1, pp. 1136–1146, 2020, https://doi.org/10.1109/TPEL.2019.2923726.

[10] Z. Liu, X. Huang, Q. Hu, G. Yang, Y. Wang and J. Shen, "Model-free predictive current control of PMSM using modified extended state observer," *IEEE Transactions on Power Electronics*, vol. 40, no. 1, pp. 679–690, 2025, https://doi.org/10.1109/TPEL.2024.3476318.

[11] K. Zhao, X. Chen, J. Liu, and J. Yu, "Discrete-time adaptive fuzzy event-triggered control for PMSMs with voltage faults via command filter approximator," *IEEE Transactions on Power Electronics*, vol. 39, no. 6, pp. 7343–7350, 2024, https://doi.org/10.1109/TPEL.2024.3369055.

[12] T.-H. Liu and Y.-H. Zhuang, "Maximum efficiency control and predictive-speed controller design for interior permanent magnet synchronous motor drive systems," *Frontiers in Electronics*, vol. 3, pp. 1–13, 2022, https://doi.org/10.3389/felec.2022.904976.

[13] J. Feng, "Parameter fuzzy rectification for sliding mode control of five-phase permanent magnet synchronous motor speed control system," *Frontiers in Mechanical Engineering*, vol. 10, pp. 1–13, 2024, https://doi.org/10.3389/fmech.2024.1391593.

[14] Q. Hou, Y. Zuo, J. Sun, C. H. T. Lee, Y. Wang, and S. Ding, "Modified nonlinear active disturbance rejection control for PMSM speed regulation with frequency domain analysis," *IEEE Transactions on Power Electronics*, vol. 38, no. 7, pp. 8126–8134, 2023, https://doi.org/10.1109/TPEL.2023.3262519.

[15] Z. Hao, Y. Yang, Y. Gong, Z. Hao, C. Zhang, H. Song, and J. Zhang, "Linear/nonlinear active disturbance rejection switching control for permanent magnet synchronous motors," *IEEE Transactions on Power Electronics*, vol. 36, no. 8, pp. 9334–9347, 2021, https://doi.org/10.1109/TPEL.2021.3055143.

[16] V. Djordjevic, H. Tao, X. Song, S. He, W. Gao, and V. Stojanovic, "Data-driven control of hydraulic servo actuator: an event-triggered adaptive dynamic programming approach," *Mathematical Biosciences and Engineering*, vol. 20, no. 5, pp. 8561–8582, 2022, https://doi.org/10.3934/mbe.2023376.

[17] J. Zhao, "Data-driven adaptive dynamic programming for optimal control of continuous-time multicontroller systems with unknown dynamics," *IEEE Access*, vol. 10, pp. 41503–41511, 2022, https://doi.org/10.1109/ACCESS.2022.3168032.

[18] T. Sun, L. Cheng, W. Wang, and Y. Pan, "Semiglobal exponential control of Euler-Lagrange systems using a sliding-mode disturbance observer," *Automatica*, vol. 112, p. 108677, 2020, https://doi.org/10.1016/j.automatica.2019.108677.

[19] M. Chen, G. Tao, and B. Jiang, "Dynamic surface control using neural networks for a class of uncertain nonlinear systems with input saturation," *IEEE Transactions on Neural Networks and Learning Systems*, vol. 26, no. 9, pp. 2086–2097, 2015, https://doi.org/10.1109/TNNLS.2014.2360933.

[20] T. Yang, N. Sun, and Y. Fang, "Adaptive fuzzy control for uncertain mechatronic systems with state estimation and input nonlinearities," *IEEE Transactions on Industrial Informatics*, vol. 18, no. 3, pp. 1770–1780, 2022, https://doi.org/10.1109/TII.2021.3089143.

[21] S. Roy, S. Baldi, and L. Fridman, "On adaptive sliding mode control without a priori bounded uncertainty," *Automatica*, vol. 111, p. 108650, 2020, https://doi.org/10.1016/j.automatica.2019.108650.

[22] Q. Deng, Y. Peng, T. Han, and D. Qu, "Event-triggered bipartite consensus in networked Euler–Lagrange systems with external disturbance," *IEEE Transactions on Circuits and Systems II: Express Briefs*, vol. 68, no. 8, pp. 2870–2874, 2021, https://doi.org/10.1109/TCSII.2021.3057859.

[23] J. Han, "From PID to active disturbance rejection control," *IEEE Transactions on Industrial Electronics*, vol. 56, no. 3, pp. 900–906, 2009, https://doi.org/10.1109/TIE.2008.2011621.

[24] W.-H. Chen, J. Yang, L. Guo, and S. Li, "Disturbance-observer-based control and related methods—An overview," *IEEE Transactions on Industrial Electronics*, vol. 63, no. 2, pp. 1083–1095, 2016, https://doi.org/10.1109/TIE.2015.2478397.

[25] W. He, Y. Sun, Z. Yan, C. Yang, Z. Li, and O. Kaynak, "Disturbance observer-based neural network control of cooperative multiple manipulators with input saturation," *IEEE Transactions on Neural Networks and Learning Systems*, vol. 31, no. 5, pp. 1735–1746, 2020, https://doi.org/10.1109/TNNLS.2019.2923241.

[26] M. Basin and P. Ramirez, "Sliding mode controller design for linear systems with unmeasured states," *Journal of the Franklin Institute*, vol. 349, no. 4, pp. 1337–1349, 2012, https://doi.org/10.1016/j.jfranklin.2011.06.019.

[27] H. Wu and P. Shi, "Adaptive variable structure state estimation for uncertain systems with persistently bounded disturbances," *International Journal of Robust and Nonlinear Control*, vol. 20, no. 17, pp. 2003–2015, 2010, https://doi.org/10.1002/rnc.1567.

[28] L. Wu, P. Shi, and H. Gao, "State estimation and sliding-mode control of Markovian jump singular systems," *IEEE Transactions on Automatic Control*, vol. 55, no. 5, pp. 1213–1219, 2010, https://doi.org/10.1109/TAC.2010.2042234.

[29] Y. Xia, H. Yang, M. Fu, and P. Shi, "Sliding mode control for linear systems with time-varying input and state delays," *Circuits, Systems, and Signal Processing*, vol. 30, no. 3, pp. 629–641, 2011, https://doi.org/10.1007/s00034-010-9237-x.

[30] İ. Eker, "Second-order sliding mode control with experimental application," *ISA Transactions*, vol. 49, no. 3, pp. 394–405, 2010, https://doi.org/10.1016/j.isatra.2010.03.010.

[31] H. F. Ho, Y. K. Wong, and A. B. Rad, "Adaptive fuzzy sliding mode control with chattering elimination for nonlinear SISO systems," *Simulation Modelling Practice and Theory*, vol. 17, pp. 1199–1210, 2009, https://doi.org/10.1016/j.simpat.2009.04.004.

[32] J. Hu, Z. Wang, H. Gao, and L. K. Stergioulas, "Robust H∞ sliding mode control for discrete time-delay systems with stochastic nonlinearities," *Journal of the Franklin Institute*, vol. 349, pp. 1459–1479, 2012, https://doi.org/10.1016/j.jfranklin.2011.05.018.

[33] T. Sun, H. Pei, Y. Pan, H. Zhou, and C. Zhang, "Neural network-based sliding mode adaptive control for robot manipulators," *Neurocomputing*, vol. 74, no. 14, pp. 2377–2384, 2011, https://doi.org/10.1016/j.neucom.2011.03.015.

[34] M. S. Kahkeshi, F. Sheikholeslam, and M. Zekri, "Design of adaptive fuzzy wavelet neural sliding mode controller for uncertain nonlinear systems," *ISA Transactions*, vol. 52, no. 3, pp. 342–350, 2013, https://doi.org/10.1016/j.isatra.2013.01.004.

[35] L. Zhang, Z. Chen, X. Yu, J. Yang, and S. Li, "Sliding-mode-based robust output regulation and its application in PMSM servo systems," *IEEE Transactions on Industrial Electronics*, vol. 70, no. 2, pp. 1852–1860, 2023, https://doi.org/10.1109/TIE.2022.3163536.

[36] X. Miao, W. Yao, H. Ouyang, and Z. Zhu, "Novel composite speed control of permanent magnet synchronous motor using integral sliding mode approach," *Mathematics*, vol. 11, no. 22, pp. 1–17, 2023, https://doi.org/10.3390/math11224666.

[37] S. Kuppusamy and Y. H. Joo, "Memory-based integral sliding-mode control for T-S fuzzy systems with PMSM via disturbance observer," *IEEE Transactions on Cybernetics*, vol. 51, no. 5, pp. 2457–2465, 2021, https://doi.org/10.1109/TCYB.2019.2953567.

[38] C. Zhang, R. Qi, B. Li, and S. Riaz, "Experimental validation and analysis of hybrid adaptive iterative learning sliding mode control for PMSM seeker coordinator," *Engineering Science and Technology, an International Journal*, vol. 58, pp. 1–11, 2024, https://doi.org/10.1016/j.jestch.2024.101826.

[39] S. H. Hosseini and M. Tabatabaei, "IPMSM velocity and current control using MTPA-based adaptive fractional order sliding mode controller," *Engineering Science and Technology, an International Journal*, vol. 20, pp. 896–908, 2017, https://doi.org/10.1016/j.jestch.2017.03.008.

[40] P. Chen and Y. Luo, "Analytical fractional-order PID controller design with Bode's ideal cutoff filter for PMSM speed servo system," *IEEE Transactions on Industrial Electronics*, vol. 70, no. 2, pp. 1783–1793, 2023, https://doi.org/10.1109/TIE.2022.3158009.

[41] L. Zhang, H. Li, L. Shan, L. Zhang, and L. Zhang, "Double-hierarchical fuzzy exponential convergence law fractional-order sliding mode control for PMSM drive control in EV," *Engineering Science and Technology, an International Journal*, vol. 47, pp. 1–13, 2023, https://doi.org/10.1016/j.jestch.2023.101536.

[42] D. Nicolis, F. Allevi, and P. Rocco, "Operational space model predictive sliding mode control for redundant manipulators," *IEEE Transactions on Robotics*, vol. 36, no. 4, pp. 1348–1355, 2020, https://doi.org/10.1109/TRO.2020.2974092.

[43] L. Wu, J. Liu, S. Vazquez, and S. K. Mazumder, "Sliding mode control in power converters and drives: A review," *IEEE/CAA Journal of Automatica Sinica*, vol. 9, no. 3, pp. 392–406, 2022, https://doi.org/10.1109/JAS.2021.1004380.

[44] S. Wang, J. Na, and Q. Chen, "Adaptive predefined performance sliding mode control of motor driving systems with disturbances," *IEEE Transactions on Energy Conversion*, vol. 36, no. 3, pp. 1931–1939, 2021, https://doi.org/10.1109/TEC.2020.3038010.

[45] J. Qiu, W. Ji, and M. Chadli, "A novel fuzzy output feedback dynamic sliding mode controller design for two-dimensional nonlinear systems," *IEEE Transactions on Fuzzy Systems*, vol. 29, no. 10, pp. 2869–2877, 2021, https://doi.org/10.1109/TFUZZ.2020.3008271.

[46] T. Orlowska-Kowalska, M. Wolkiewicz, P. Pietrzak, M. Skowron, P. Ewert, G. Tarchala, M. Krzysztofiak, and C. T. Kowalski, "Fault diagnosis and fault-tolerant control of PMSM drives – state of the art and future challenges," *IEEE Access*, vol. 10, pp. 59979–60024, 2022, https://doi.org/10.1109/ACCESS.2022.3180153.

[47] A. Najem, A. Moutabir, A. Ouchatti, and M. Haissouf, "Experimental validation of the generation of direct and quadratic reference currents by combining the ant colony optimization algorithm and sliding mode control in PMSM using the process PIL," *International Journal of Robotics and Control Systems*, vol. 4, no. 1, pp. 188–216, 2024, https://doi.org/10.31763/ijrcs.v4i1.1286.

[48] L. Wang, J. Mishra, Y. Zhu, and X. Yu, "An improved sliding-mode current control of induction machine in presence of voltage constraints," *IEEE Transactions on Industrial Informatics*, vol. 16, no. 2, pp. 1182–1191, 2020, https://doi.org/10.1109/TII.2019.2944228.

[49] M. S. Hassan, A. F. Khan, M. W. Khan, M. Uzair, and K. Khurshid, "A computationally low cost vision-based tracking algorithm for human-following robot," in *Proc. 2016 2nd International Conference on Control, Automation and Robotics (ICCAR)*, 2016, pp. 62–65, https://doi.org/10.1109/ICCAR.2016.7486699.

[50] M. Vanitha, M. Selvalakshmi, and R. Selvarasu, "Monitoring and controlling of mobile robot via internet through Raspberry Pi board," in *Proc. 2016 Second International Conference on Science Technology Engineering and Management (ICONSTEM)*, 2016, pp. 462–466, https://doi.org/10.1109/ICONSTEM.2016.7560864.

[51] R. Szabo and A. Gontean, "Industrial robotic automation with Raspberry Pi using image processing," in *Proc. 2016 International Conference on Applied Electronics (AE)*, 2016, pp. 265–268, https://doi.org/10.1109/AE.2016.7577287.

[52] R. Szabo and A. Gontean, "Robotic arm control algorithm based on stereo vision using RoboRealm vision," *Advances in Electrical and Computer Engineering*, vol. 15, no. 2, pp. 65–74, 2015, https://doi.org/10.4316/AECE.2015.02009.

[53] B. V. S. Krishna, J. Oviya, S. Gowri, and M. Varshini, "Cloud robotics in industry using Raspberry Pi," in *Proc. 2016 Second International Conference on Science Technology Engineering and Management (ICONSTEM)*, 2016, pp. 543–547, https://doi.org/10.1109/ICONSTEM.2016.7560952.

[54] K. Premkumar and K. G. J. Nigel, "Smart phone-based robotic arm control using Raspberry Pi, Android and Wi-Fi," in *Proc. 2015 International Conference on Innovations in Information, Embedded and Communication Systems (ICIIECS)*, 2015, pp. 1–3, https://doi.org/10.1109/ICIIECS.2015.7192973.

[55] P. Siagian and K. Shinoda, "Web-based monitoring and control of robotic arm using Raspberry Pi," in *Proc. 2015 International Conference on Science in Information Technology (ICSITech)*, 2015, pp. 192–196, https://doi.org/10.1109/ICSITech.2015.7407802.

[56] D. Hernandez, H. Trejo, and E. Ordonez, "Development of an exploration land robot using low-cost and open-source platforms for educational purposes," *Journal of Physics: Conference Series*, vol. 582, p. 012007, 2015, https://doi.org/10.1088/1742-6596/582/1/012007.

[57] A. D. Diallo, S. Gobee, and V. Durairajah, "Autonomous tour guide robot using embedded system control," *Procedia Computer Science*, vol. 76, pp. 126–133, 2015, https://doi.org/10.1016/j.procs.2015.12.302.

[58] N. Ollukaren and K. McFall, "Low-cost platform for autonomous ground vehicle research," in *Proc. 14th Early Career Technical Conference*, 2014, https://facultyweb.kennesaw.edu/kmcfall/2014ECTC2.pdf.

[59] H. Kareemullah, D. Najumnissa, M. M. Shajahan, M. Abhineshjayram, V. Mohan, and S. A. Sheerin, "Robotic Arm controlled using IoT application," *Computers and Electrical Engineering*, vol. 105, p. 108539, 2023, https://doi.org/10.1016/j.compeleceng.2022.108539.

[60] S. Seshagiri and H. K. Khalil, "Output feedback control of nonlinear systems using RBF neural networks," *IEEE Transactions on Neural Networks*, vol. 11, no. 1, pp. 69–79, 2000, https://doi.org/10.1109/72.822511.

[61] T. H. Tran, T. Q. Ngo, H. T. T. Uyen, V. T. Nguyen, and T. D. Duong, "Adaptive task-space control of five-bar parallel robot dynamic model with fully unknown parameters using radial basis function neural networks for high-precision applications," *Journal of Robotics and Control*, vol. 6, no. 4, pp. 1624–1635, Jun. 2025, https://doi.org/10.18196/jrc.v6i4.26537.

[62] P. Pillay and R. Krishnan, "Modeling of permanent magnet motor drives," *IEEE Transactions on Industrial Electronics*, vol. 35, no. 4, pp. 537–541, 1988, https://doi.org/10.1109/41.9176.

[63] W. Leonhard, *Control of Electrical Drives*, 2nd ed. Berlin: Springer, 1995, https://doi.org/10.1007/978-3-642-97646-9.

[64] J. Zhou and Y. Wang, "Real-time nonlinear adaptive backstepping speed control for a PM synchronous motor," *Control Engineering Practice*, vol. 13, no. 10, pp. 1259–1269, Oct. 2005, https://doi.org/10.1016/j.conengprac.2004.11.007.